Facile Synthesis and Characterization of Molybdenum Carbides/Carbon Nanocomposites by Laser Pyrolysis

Théo Caroff, Pitalinani Badaki, Nathalie Herbert, Franck Tessier, David Berthebaud, Naoki Ohashi, Tetsuo Uchikoshi, Pierre Lonchambon, Nathalie Herlin-Boime, Fabien Grasset

HAL Id: cea-03755521

https://cea.hal.science/cea-03755521

Submitted on 22 Aug 2022

Communication

Facile Synthesis and Characterization of Molybdenum Carbides/Carbon Nanocomposites by Laser Pyrolysis

Théo Caroff [1,2,3], Pitalinani Badaki [3,4], Nathalie Herbert [4], Franck Tessier [4], David Berthebaud [1,2], Naoki Ohashi [1,2], Tetsuo Uchikoshi [1,2], Pierre Lonchambon [3], Nathalie Herlin-Boime [3,*] and Fabien Grasset [1,4,*]

1 CNRS-Saint-Gobain-NIMS, IRL 3629, Laboratory for Innovative Key Materials and Structures (LINK), NIMS, Tsukuba 305-0044, Japan
2 Research Center for Functional Materials, National Institute for Materials Science (NIMS), Tsukuba 305-0044, Japan
3 CEA, IRAMIS UMR NIMBE, Université Paris Saclay, F-91191 Gif-Sur-Yvette, France
4 Univ Rennes, CNRS, ISCR (Institut des Sciences Chimiques de Rennes)–UMR6226, F-35000 Rennes, France
* Correspondence: nathalie.herlin@cea.fr (N.H.-B.); fabien.grasset@univ-rennes1.fr (F.G.)

Abstract: This short communication reports on the facile and scalable synthesis and characterization of molybdenum carbides/carbon nanocomposites prepared by laser pyrolysis in a one-step process. Water and commercial molybdenum oxide were used as low-cost environmentally friendly precursors. The nanocomposites are mainly composed of two types of carbides with different apparent crystallite sizes, 21 ± 1 nm and 9 ± 1 nm for Mo_2C and MoC_{1-x}, respectively. Thanks to a simple annealing at 500 °C under argon, it was possible to increase the specific surface area around 50 m^2/g without changing the morphology of the nanocomposite.

Keywords: nanocomposites; molybdenum carbides; laser pyrolysis

1. Introduction

H_2 or dihydrogen (hydrogen for short) is a very promising energy carrier with many potential technological developments [1]. It could be converted into electricity, heat, or motive force and has, thus, many applications. Moreover, the generated power from its combustion is three-times more than gasoline for an equivalent weight [2]. Moreover, its combustion does not produce CO_2. However, hydrogen is rather difficult to store and to transport due to its low energy density per volume unit. In addition, hydrogen is generally produced from natural gas, and the process emits a large amount of CO_2 to the atmosphere, making the technology hardly compatible with the current environmental concerns. It is of paramount importance to develop sustainable technologies for the production of hydrogen such as biomass conversion or water splitting [1,3,4]. These methods allow the production of cleaner, safer, and more sustainable hydrogen, but unfortunately, the hydrogen produced through the water splitting process is less than 4% compared to the overall H_2 industrial production in the world [4]. An efficient water splitting process, such as electrocatalysis, generally employs noble metals (Pd, Ir, Pt, etc.), whose resources are expensive, scarce, and already used in many other applications [5]. These points enhance the need to develop cost-effective catalysts for the large-scale implementation of hydrogen technology. Indeed, all the water splitting processes, including thermolysis, photolysis, and electrolysis, are to date the most expensive on the market with a cost of H_2 around EUR 8–10/kg [4]. The search for alternative catalysts to noble metals for electrocatalysis and with good markers of energy policies (availability, accessibility, affordability, and acceptability) is essential for the production of renewable hydrogen or even the use of hydrogen for fuel cells as a replacement of thermal engines. In this context, transition-metal-based boride, carbide, nitride, and sulfide materials are very promising and are currently attracting a growing

interest in the energy field [6–11]. Especially the molybdenum borides, carbides, and nitrides seem to be a suitable compromise for catalytic applications for green hydrogen production and applications [6,12–21]. Moreover, Mo is not classified as critical material by the European Union [22].

Such Mo-based materials are usually synthesized by chemical methods, as detailed in a review paper by Ma et al. [6]. In this short communication, we report on laser pyrolysis as an alternative method for the facile and scalable synthesis of molybdenum carbides/carbon nanocomposites (Mo_yC/GCs). The objective of this study is to evaluate the potential of laser pyrolysis for the production of molybdenum carbide nanocomposites. Utilizing water and commercial molybdenum oxide as low-cost, environmentally friendly precursors, we prepared, for the first time, molybdenum carbide nanoparticles dispersed in carbon via a one-step reaction by the laser pyrolysis process.

2. Materials and Methods

2.1. Chemicals

Commercial ammonium heptamolydate tetrahydrate, $(NH_4)_6Mo_7O_{24}\cdot 4H_2O$, was purchased from Sigma Aldrich (St. Louis, MO, USA) (USP specifications, reference A1343). C_2H_4 and NH_3 were purchased from Air Liquide and Air Product, respectively. All chemicals were used without purification. The deionized water was obtained from the MilliQ equipment from Merck with a conductance of 10^{-4} S m^{-1} at 25 °C. $(NH_4)_6Mo_7O_{24}\cdot 4H_2O$ was simply solubilized at room temperature by magnetic stirring in water at a concentration of 50 g/L. Two different solutions were prepared without urea (called Solution A) and with urea (called Solution B) (31 g of urea was added to Solution B).

2.2. Synthesis of Mo_yC/GC Nanocomposites

To synthesize these Mo_yC/GC nanocomposites containing molybdenum carbides, we used a laser pyrolysis process, which is an original method invented at the Massachusetts Institute of Technology [23]. Indeed, the synthesis by laser pyrolysis is a continuous process that generally leads to a production rate of several grams per hour [23]. The method was initially developed with the use of gaseous precursors and was extended to liquid precursors [24,25]. Its principle is based on the resonant interaction between a high-power infrared laser and a precursor, carried into the reactor zone thanks to an inert gas. The experimental device used in these experiments mainly consisted of a high-power CO_2 laser ($\lambda = 10.6$ μm) and an optical path, a reaction chamber, a gas delivery system, and pyrosol, which allows the use of a liquid precursor. In this study, the CO_2 laser power was set to 1500 W (i.e., 70% of internal power), and the pressure in the reactor was maintained at atmospheric pressure (1.013×10^5 Pa). The temperature of the flame was estimated with an IR camera (Pyroview 512N). The liquid precursor was contained in a glass jar equipped with an ultrasonic generator (pyrosol device from RBI, Meylan, France). An aerosol composed of precursor droplets was produced in this pyrosol. Indeed, the ultrasound generator destroyed the surface of the liquid and created very tiny droplets. The cloud of droplets was carried in the reaction chamber by the argon gas (600 sccm). A sensitizer gas, C_2H_4 and/or NH_3, was added to the carrier gas in our case, as a precursor does not absorb the laser radiation at 10.6 μm. When the precursor interacted with the laser beam, it was heated, and collisional energy transfer caused a rise in temperature in the reaction zone, allowing dissociation of the precursor molecules with the appearance of a flame, in which the nanoparticles formed almost instantly.

2.3. Characterization

X-ray diffraction (XRD): Patterns were recorded in the 20–80° 2θ range on a Bruker (Billerica, MA, USA) D2 Phaser (Cu Kα, 30 kV, 10 mA) diffractometer equipped with an SSD160^{TM} detector. Le Bail-type refinements were conducted using the FullProf Suite software using profile matching mode.

The X-ray data for refinements were recorded on a Rigaku XRD (Rigaku Corp., Tokyo, Japan) with a Cu cathode without a monochromator. The instrumental resolution function was evaluated by using a monocrystal of silicium.

Carbon elemental analyses: Carbon content was measured with an EMIA analyzer from the HORIBA company (Edison, NJ, USA).

Thermogravimetric analysis (TGA): The TGA analysis was carried out on a TGA55 of the TA Instruments brand (New Castle, DE, USA). The maximum operating temperature is 1000 °C. Measurements were performed in air, with a flow rate of 90 mL/min. For each of the samples, we chose a ramp of 10 °C/min from room temperature up to 1000 °C, then an isotherm of 30 min, and finally, a slow decrease of the unprogrammed temperature to room temperature.

Specific surface area (SSA): The Brunauer−Emmet−Teller (BET) specific surface area was determined from nitrogen physisorption with a Micromeritics (Norcross, GA, USA) Gemini VII 2390t instrument using a mixture of N_2/He (30%/70%). To avoid the surface hydration and remove the polycyclic aromatic hydrocarbon (PAH) contaminants, samples were previously outgassed under a vacuum at 150 °C.

Scanning and transmission electron microscopy (SEM and TEM): SEM photographs were taken by using a JEOL JSM 7100F (JEOL, Ltd., Tokyo, Japan) operating at 10 kV to examine the microstructure (shape and size) of the nanocomposites. Compositional analyses were performed by energy dispersive X-ray spectroscopy (EDS) with EDS SDD X-Max (50 mm^2) Oxford Instruments (Abingdon-on-Thames, UK) AZtecEnergy detectors. High-resolution TEM images (HRTEM), scanning transmission electron microscopy (STEM) images, and energy dispersive (EDX) spectra or maps were acquired by using a high-resolution transmission electron microscope, JEOL JEM 2100F (JEOL, Ltd., Tokyo, Japan). An acceleration tension of 200 kV was used to estimate the crystallinity and morphology of the carbide's nanoparticles. For SEM analysis, the powder was directly observed on the carbon tape. For HRTEM measurements, a small amount of powder was dispersed in ethanol by using ultrasound. Then, the dispersion was dropped on a net-like carbon-film-covered Cu grid (Cu micro grid) and dried in ambient conditions.

3. Results and Discussion

As mentioned in the Introduction, molybdenum carbide has been attracting more and more attention as a potential electrocatalyst for HER. This is mainly due to some advantages such as the unique surface and electronic properties, high catalytic activity, high selectivity, high sulfur and nitrogen tolerance, and low cost, compared to Pt-group metal catalysts [6]. Dispersing molybdenum carbide nanoparticles on a conductive substrate is a commonly used strategy to optimize the performance of HER catalyst. Consequently, facile, scalable, and low-cost synthesis of small-sized, well-dispersed, and electrochemically accessible Mo_2C nanoparticles therefore remains challenging at the present time [26]. The direct synthesis of carbon nanocomposites containing molybdenum carbides for HER has been already achieved by several groups; most of them used the carburization of Mo precursors and carbon sources at a high temperature (700 °C < T < 1000 °C) mainly under an argon or N_2 atmosphere [13–15,21,27–35]. Other alternatives reported in the literature include CVD, where large-area 2D Mo_2C/graphene heterostructures were prepared [36].

In this study, the synthesis of the Mo_yC/GC nanocomposites was performed in a one-step method by laser pyrolysis. To the best of our knowledge, only a few papers from the same group already reported more than 25 years ago the synthesis by laser pyrolysis of (oxy)carbide/nitride powders by using $Mo(CO)_6$ as precursors [37–39]. In their particular process, the carburizing (C_2H_4) gas passed through a sublimation cell containing the solid precursors ($Mo(CO)_6$, which is quite toxic due to CO evolution. A new and very important point of this study is that the Mo_yC/GCs powders were obtained from an easy-to-use commercial oxide precursor, $(NH_4)_6Mo_7O_{24}\cdot4H_2O$, dispersed in water and used as a liquid precursor. The as-formed nanocomposites are black in color. This color is attributed to carbides and also to a significant amount of residual carbon phases due

to the decomposition of the gas sensitizer (mainly C_2H_4), as expected. The characteristic composition of the obtained nanocomposite could be tuned by the choice of experimental conditions (including laser power, reactor pressure, and gas flow rate). The most relevant experimental conditions are reported in Table 1 using the two solutions of the precursors labelled A and B. Table 1 shows that the presence of carbon is high in all samples, from 68 to 86 wt%, well correlated with the C_2H_4 flow: 80% C content corresponds to a gas flow rate of 200 sccm for C_2H_4, while about 70 wt% was obtained with a gas flow rate of 100 sccm. In the same way, the production rate is higher when the C_2H_4 gas flow rate is high (700–800 mg/hour vs. 180–250 mg/hour). The production rate significantly decreases when NH_3 is added in the reactive mixture, in connection probably with a less-efficient decomposition of precursors and less-efficient transfer of droplets. The presence of urea tends to increase the production without a significant change in the carbon content.

Table 1. Most relevant experimental conditions.

Synthesis Number	Solution	CO_2 Laser Power (W)	C_2H_4 (sccm)	NH_3 (sccm)	Total Production (mg/h) (± 1)	% Carbon Elemental Analysis * (± 1)
MOC4	A	1475	200	0	694	86
MOC5	A	1475	100	0	180	68
MOC6	B	1477	200	0	827	85
MOC7	B	1477	100	0	225	71
MOC8	B	1477	130	0	253	77
MOC9	B	1568	100	0	237	71
MOC10	B	1568	100	100	200	74
MOC11	B	1527	50	100	67	n.m.
MOC12	B	1527	0	200	8	n.m.

* wt%, measured by an EMIA analyzer, not measured (n.m.) for Samples 11 and 12 due to the low amount of material. "Laser power" is the power measured by the power meter before initiation of the reaction (i.e., only in the presence of neutral gases).

Heat treatments were carried out in air or argon in order to study the thermal behavior of the Mo_yC/GCs samples and to evaluate the mass percentage of free carbon present in the sample in connection with carbon elemental analysis. Analysis of the curves obtained by TGA showed similar patterns for all the samples in both atmospheres (Figures S1 and S2).

Under air, a slight loss in mass of about 10% was observed at a low temperature (<300 °C) due mainly to the desorption of the adsorbed compounds as mostly hydrocarbon aromatic polycyclic (HAP). Between 300 °C and 350 °C, there was a rapid drop in mass linked to the loss of free carbon. This loss of free carbon represents around 70% to 80% of the total mass loss depending on the sample, which confirmed the large amount of free carbon in all the samples as estimated by carbon elemental analysis. At the same time, the weight loss should also be decreased a bit by the oxidation process of the carbides. This point was confirmed by XRD analysis after a thermal treatment in air at 500 °C, which shows that the samples consist almost entirely of oxides of MoO_3 and MoO_2 (Figure S3). From 700 °C to almost 1000 °C, a new drop in mass was observed, probably related to the sublimation of MoO_3.

Under argon, a slight loss in mass of around 10% was also observed, but until 450 °C, followed by a slow decrease of the mass up to 1000 °C due to the carbon loss.

The average value of the SSA was measured around 20 m²/g (± 2 m²/g) for all the Mo_yC/GCs samples with an average pore radius <40 nm, whatever the experimental conditions. The SSA increased to 47 m²/g after annealing the samples at 500 °C for 3 h under an argon atmosphere (and the average radius pore size decreased to 4 nm), which could be explained by a full removal of HAP.

Analysis of the powder XRD results showed that each powder was composed of a mixture of crystallized phases. Indeed, all XRD patterns (except MOC12) can be indexed as a mixture of oxide and carbide phases (Figure S4). The main peaks observed at 26°, 39°, and 43° correspond, respectively, to the oxide and to the two types of carbides. The peak obtained at 26° is attributed to MoO_2; that obtained at 39° is attributed to the β-Mo_2C-type carbide; that at 43° is attributed to the MoC_{1-x}-type carbide. The best result (i.e., with a very low content of oxide phase) was obtained for MOC10 by using an equal mixture of C_2H_4 and NH_3 gases as sensitizer gases and B solution. In the case of MOC12 with only NH_3 as the sensitizer gas, the MoN phase can be detected as one of the main phases.

In order to have a better understanding of the microstructure of the Mo_yC/GCs samples, we used the Fullprof suite software including WinPlotr to perform crystallite size refinements on the MOC10 sample [40,41]. The Thompson–Cox–Hastings pseudo-Voigt function (Npr = 7) was used to fit the X-ray data. The background was determined by Fullprof under the form of manually selected points, which were interpolated. The first cell parameters used for the refinement were extracted from the ICSD database.

The refinement strategy is:

- Start without refining parameters to generate the hkl information.
- Refine the lattice parameter.
- Refine the Y parameter and GauSize.

The estimation of the crystallite size assumed an isotropic model without strain contributions. These estimations were directly calculated by FullProf using Scherrer's equation.

The refinement shown in Figure 1 provides these results:

- Average apparent size for MoC_{1-x} *phase* : 9 nm (±1 nm);

- Average apparent size for Mo_2C *phase* : 21 nm (± 1 nm).
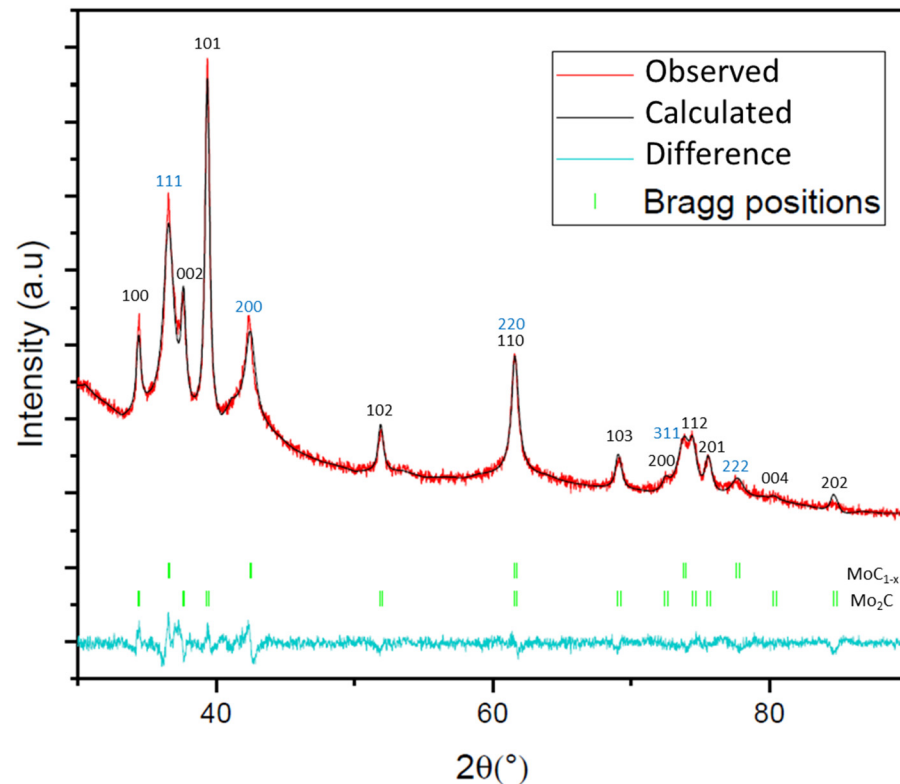
Figure 1. Observed (red line), calculated (black line), and difference (blue line) X-ray powder diffraction profiles of the MOC10 sample. hkl indexes for Mo_2C (black) and MoC_{1-x} (blue). The oxide phase was not included in the refinement.

We clearly demonstrated that the nanocomposite MOC10 is mainly composed of two types of carbides with different apparent crystallite sizes: the Mo_2C phase is larger (around 2.3-times) than the MoC_{1-x} phase. Regarding the powder XRD results, we assumed that this conclusion can be extended to all samples.

The morphologies and chemical composition of the nanocomposite powders were also studied by SEM and EDX analysis. Figure 2 shows an overview of the general aspect of the powders and confirms the heterogeneity of the samples. For all the samples (except MOC12), we observed similar spherical bright spots dispersed in a dark background (Figure 2a). The average diameter of these bright spots was below 1 μm. The morphology of the nanocomposite, and especially these spherical particles, remained similar even after annealing at 500 °C under argon (Figures S5 and S6). A zoom on these spherical bright spots (represented by the white rectangle in Figure 2a) is presented in Figure 2b–d with different magnifications. We can clearly observe that these spots are spherical grains, which are composed of several aggregated nanoparticles (Figure 2d). The EDX analysis (point mode) indicated clearly the presence of molybdenum in these aggregates.
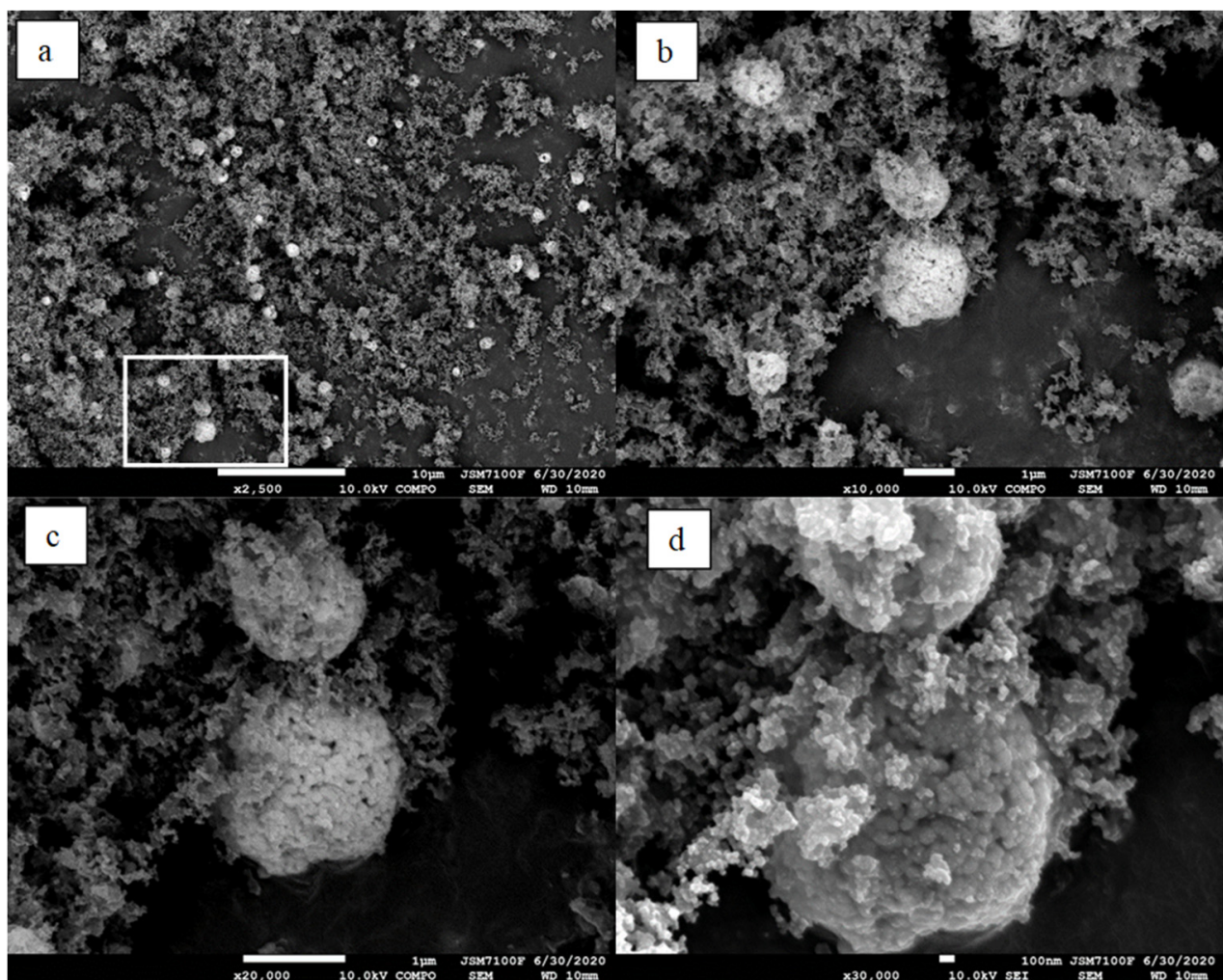
Figure 2. (**a–d**) Examples of SEM images of MOC10 nanocomposites. Scale bar sizes: (**a**) 10 μm, (**b**) 1 μm, (**c**) 1 μm, (**d**) 100 nm.

To better investigate the nanocomposites and especially the aggregated nanoparticles, we used a high-resolution transmission electron microscope. HRTEM and selected area electron diffraction (SAED) were performed on the sample to verify the crystallinity and to confirm the data obtained by powder XRD (Figure 3). Well-crystallized particles were observed by TEM (Figure 3 left), and the SAED pattern consisted of wide diffraction circles, as expected, characteristics of aggregated nanocrystals (Figure 3 right). A very interesting point is that the aggregates observed by HRTEM appeared to be empty and looked like hollow spheres more than dense particles, something that was not expected from the SEM analysis.
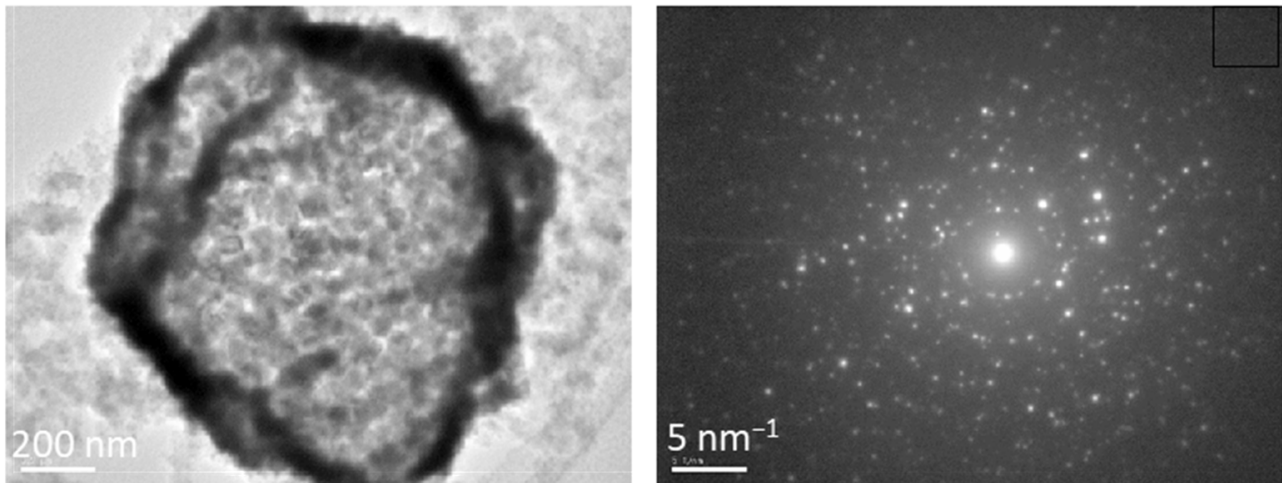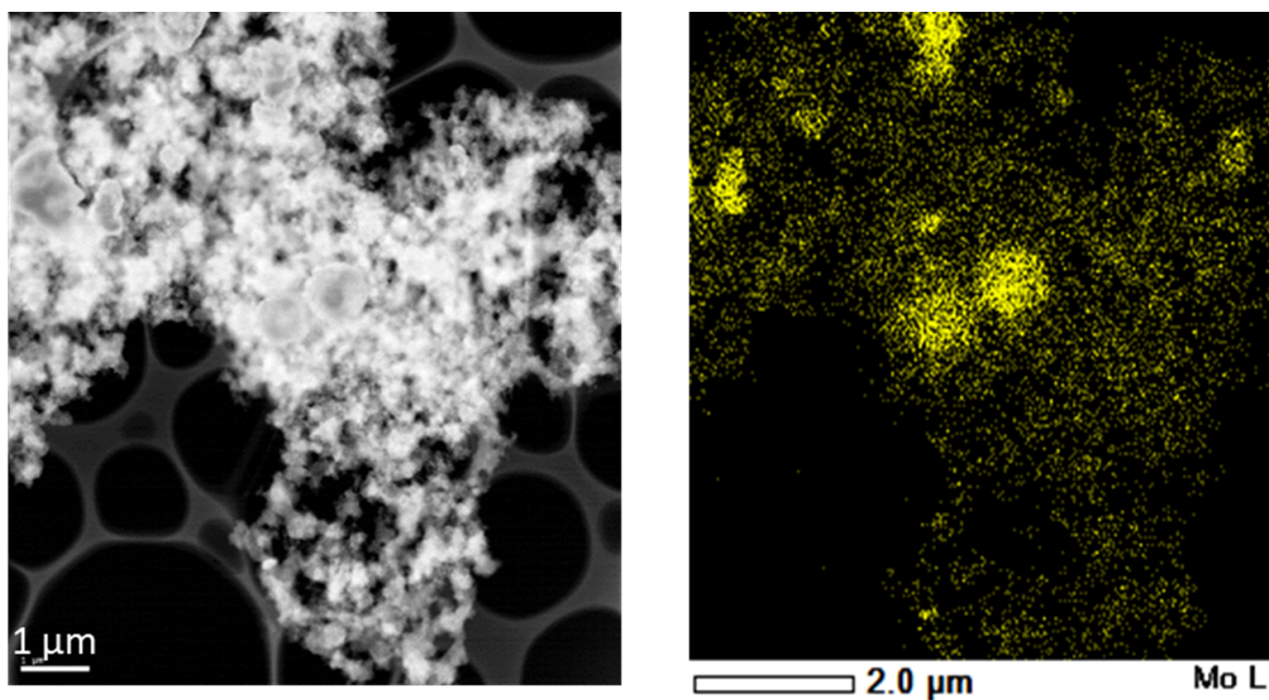

Figure 3. HRTEM (**left**) image of the MOC10 sample and SAED (**right**) pattern.

This last point was clearly confirmed by the STEM-EDX images (Figure 4). In Figure 5 right, unlike the core, we observed a Mo-enriched shell. Nevertheless, on the same mesh copper grid, a careful analysis of the STEM-EDX experiments indicated that molybdenum was not only concentrated in the micron-size aggregates, but also quite dispersed in all the nanocomposite (Figure 5). Indeed, a deep study by HRTEM revealed without ambiguities the presence of numerous nanocrystals containing molybdenum concomitantly to the spherical aggregates' formation. Their sizes varied from 3 nm to 10 nm (Figure 6a,b), and the d-spacing value was estimated at 1.24 Å, which is comparable to the (222) plane of MoC_{1-x} or even to the (201) plane of Mo_2C. The EDX analysis of the area containing the nanocrystals confirmed the presence of molybdenum (Figure 6c). Most were agglomerated and visible even at lower magnification. Regarding the XRD refinement, we can suppose that the bigger hollow particles are mainly formed by Mo_2C nanocrystals and the smaller nanocrystals dispersed in carbon by the MoC_{1-x} phase. Of course, because the crystallized parts were systematically coated with a large amount of amorphous carbon, it is very complicated to confirm this hypothesis. A very important point is that these nanocrystals and nanoparticles remained present even after the annealing process at 500 °C under argon (Figure S6).
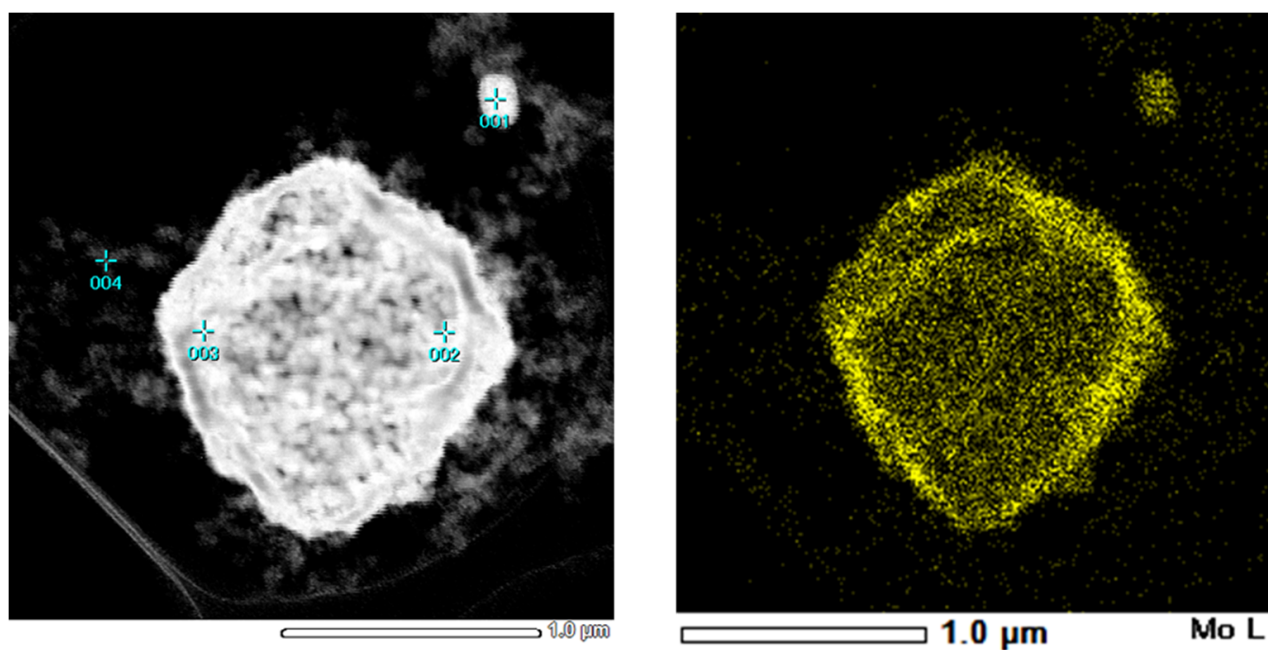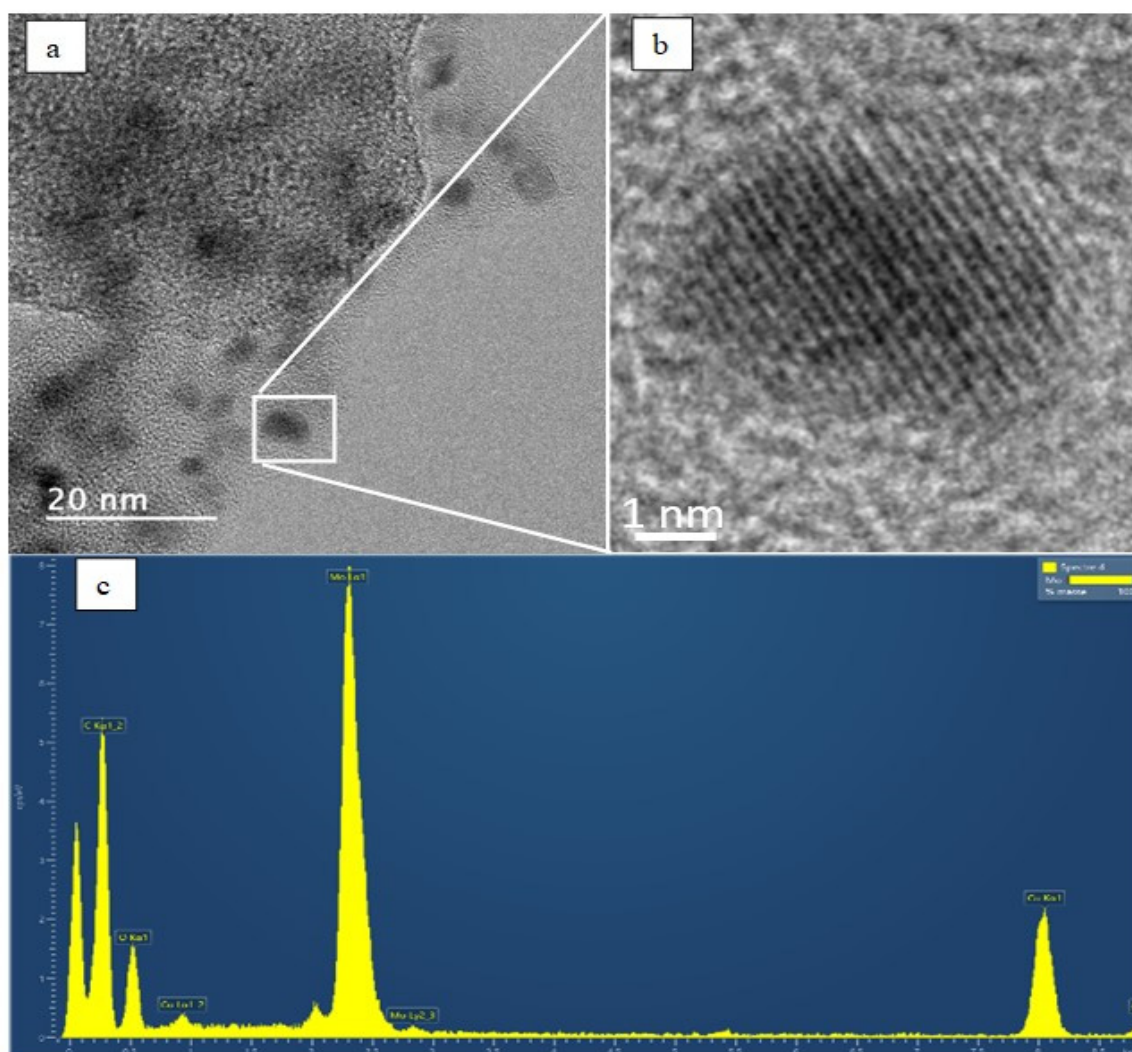
Figure 4. STEM (**left**) and EDX (**right**) mapping images of a single MOC10 aggregate. Mo appears in yellow color.

Figure 5. STEM (**left**) and EDX (**right**) mapping images of a large area of the MOC10 sample. Mo appears in yellow color.

All these SEM and HRTEM analyses confirmed the XRD results and the composite composition of the samples.

Figure 6. (**a**,**b**) HRTEM images and (**c**) EDX mapping image of the MOC10 sample.

4. Conclusions

The studies carried out in this exploratory study on laser pyrolysis synthesis clearly demonstrate the possibility to obtain large amounts of molybdenum carbides/carbon nanocomposites by using water as a solvent and a safe and low-cost oxide precursor. This one-step process led at the best to a mixture with at least two phases of carbides, including the hex-Mo_2C compound, which has the best catalytic performance for the HER reaction reported in the literature [6], and the fcc-MoC_{1-x} compound, which interestingly exhibits a higher water dissociation ability, producing abundant surface OH^-, which promotes the reforming of intermediates in the reaction at the surface [42–44]. The crystallized parts of the nanocomposites are mainly composed of two types of carbides with different apparent crystallite sizes, 21 nm $\pm$ 1 nm and 9 nm $\pm$ 1 nm for Mo_2C and MoC_{1-x}, respectively. A high carbon content containing HAP was generated in the compounds, and to reduce it, annealing was necessary. Thanks to a simple annealing at 500 °C under argon, it was possible to increase the SSA around 50 m^2/g without changing the morphology of the nanocomposite. The next step will be to perform HER catalytic experiments.

Supplementary Materials: The following Supporting Information can be downloaded at: https://www.mdpi.com/article/10.3390/nanomanufacturing2030009/s1, Figure S1: TGA of MOC9 under air; Figure S2: TGA of MOC9 under air; Figure S3: XRD patterns of MOC9@500 °C under air; Figure S4. Powder XRD patterns of MOCX (5 < X < 12) obtained on a sample without any treatment.

The references plotted in the figure were obtained from the Eva data source software available on the DRX apparatus; Figure S5. SEM image of MOC10 after annealing at 500 °C under argon; Figure S6. HRTEM image of MOC10 after annealing at 500 °C under argon.

Author Contributions: T.C. and P.B. contributed equally. T.C., P.B. and P.L. performed the synthesis and characterization experiments of Mo_yC/GCs by laser pyrolysis. N.H. performed the BET experiments. D.B. performed the XRD refinement. F.T., D.B., N.O. and T.U. revised the manuscript. N.H.-B. and F.G. conceived and designed the project; analyzed and interpreted the data; and drafted the article. All authors have read and agreed to the published version of the manuscript.

Institutional Review Board Statement: Not applicable.

Informed Consent Statement: Not applicable.

Data Availability Statement: Not applicable.

Conflicts of Interest: The authors declare no conflict of interest.

References

1. Okolie, J.A.; Patra, B.R.; Mukherjee, A.; Nanda, S.; Dalai, A.K.; Kozinski, J.A. Futuristic applications of hydrogen in energy, biorefining, aerospace, pharmaceuticals and metallurgy. *Int. J. Hydrogen Energy* **2021**, *46*, 8885. [CrossRef]
2. Nanda, S.; Rana, R.; Zheng, Y.; Kozinski, J.A.; Dalai, A.K. Insights on pathways for hydrogen generation from ethanol. *Sustain. Energy Fuels* **2017**, *1*, 1232. [CrossRef]
3. Wang, Q.; Domen, K. Particulate photocatalysts for light-driven water splitting: Mechanisms, challenges, and design strategies. *Chem. Rev.* **2020**, *120*, 919. [CrossRef] [PubMed]
4. Shiva Kumar, S.; Himabindu, V. Hydrogen production by PEM water electrolysis—A review. *Mater. Sci. Energy Technol.* **2019**, *2*, 442. [CrossRef]
5. Renner, H.; Schlamp, G.; Kleinwächter, I.; Drost, E.; Lüschow, H.M.; Tews, P.; Panster, P.; Diehl, M.; Lang, J.; Kreuzer, T.; et al. Platinum group metals and compounds. In *Ullmann's Encyclopedia of Industrial Chemistry*; Wiley: Hoboken, NJ, USA, 2018.
6. Ma, Y.; Guan, G.; Hao, X.; Cao, J.; Abudula, A. Molybdenum carbide as alternative catalyst for hydrogen production—A review. *Renew. Sustain. Energy Rev.* **2017**, *75*, 1101. [CrossRef]
7. Guo, Y.; Park, T.; Yi, J.W.; Henzie, J.; Kim, J.; Wang, Z.; Jiang, B.; Bando, Y.; Sugahara, Y.; Tang, J.; et al. Nanoarchitectonics for Transition-Metal-Sulfide-Based Electrocatalysts for Water Splitting. *Adv. Mater.* **2019**, *31*, 1807134. [CrossRef] [PubMed]
8. Hua, W.; Sun, H.H.; Xu, F.; Wang, J.G. A review and perspective on molybdenum-based electrocatalysts for hydrogen evolution reaction. *Rare Met.* **2020**, *39*, 335. [CrossRef]
9. Wang, H.; Li, J.; Li, K.; Lin, Y.; Chen, J.; Gao, L.; Nicolosi, V.; Xiao, X.; Lee, J.M. Transition metal nitrides for electrochemical energy applications. *Chem. Soc. Rev.* **2021**, *50*, 1354. [CrossRef]
10. Chen, H.; Zou, X. Intermetallic borides: Structures, synthesis and applications in electrocatalysis. *Inorg. Chem. Front.* **2020**, *7*, 2248. [CrossRef]
11. Gujral, H.S.; Singh, G.; Baskar, A.V.; Guan, X.; Geng, X.; Kotkondawar, A.V.; Rayalu, S.; Kumar, P.; Karakoti, A.; Vinu, A. Metal nitride-based nanostructures for electrochemical and photocatalytic hydrogen production. *Sci. Technol. Adv. Mater.* **2022**, *23*, 76. [CrossRef]
12. Vrubel, H.; Hu, X. Molybdenum boride and carbide catalyze hydrogen evolution in both acidic and basic solutions. *Angew. Chem.* **2012**, *124*, 12875. [CrossRef]
13. Youn, D.H.; Han, S.; Kim, J.Y.; Kim, J.Y.; Park, H.; Choi, S.H.; Lee, J.S. Highly active and stable hydrogen evolution electrocatalysts based on molybdenum compounds on carbon nanotube–graphene hybrid support. *ACS Nano* **2014**, *8*, 5164. [CrossRef] [PubMed]

14. Cui, W.; Cheng, N.; Liu, Q.; Ge, C.; Asiri, A.M.; Sun, X. Mo$_2$C nanoparticles decorated graphitic carbon sheets: Biopolymer-derived solid-state synthesis and application as an efficient electrocatalyst for hydrogen generation. *ACS Catal.* **2014**, *4*, 2658. [CrossRef]

15. Huang, Y.; Gong, Q.; Song, X.; Feng, K.; Nie, K.; Zhao, F.; Wang, Y.; Zeng, M.; Zhong, J.; Li, Y. Mo$_2$C nanoparticles dispersed on hierarchical carbon microflowers for efficient electrocatalytic hydrogen evolution. *ACS Nano* **2016**, *10*, 11337. [CrossRef] [PubMed]

16. Lv, C.; Huang, Z.; Yang, Q.; Wei, G.; Chen, Z.; Humphrey, M.G.; Zhang, C. Ultrafast synthesis of molybdenum carbide nanoparticles for efficient hydrogen generation. *J. Mater. Chem. A* **2017**, *5*, 22805. [CrossRef]

17. Kumar, R.; Rai, R.; Gautam, S.; De Sarkar, A.; Tiwari, N.; Nath Jha, S.; Bhattacharya, D. Nano-structured hybrid molybdenum carbides/nitrides generated in situ for HER applications. *J. Mater. Chem. A* **2017**, *5*, 7764. [CrossRef]

18. Jothi, P.R.; Zhang, Y.; Scheifers, J.P.; Park, H.; Fokwa, B.P.T. Molybdenum diboride nanoparticles as a highly efficient electrocatalyst for the hydrogen evolution reaction. *Sustain. Energy Fuels* **2017**, *1*, 1928. [CrossRef]

19. Jin, H.; Liu, X.; Vasileff, A.; Jiao, Y.; Zhao, Y.; Zheng, Y.; Qiao, S.Z. Single-crystal nitrogen-rich two-dimensional Mo$_5$N$_6$ nanosheets for efficient and stable seawater splitting. *ACS Nano* **2018**, *12*, 12761. [CrossRef]

20. Guy, K.; Tessier, F.; Kaper, H.; Grasset, F.; Dumait, N.; Demange, V.; Nishio, M.; Matsushita, Y.; Matsui, Y.; Takei, T.; et al. Original synthesis of molybdenum nitrides using metal cluster compounds as precursors: Applications in heterogeneous catalysis. *Chem. Mater.* **2020**, *32*, 6026. [CrossRef]

21. Wang, L.; Zhao, S.; Liu, Y.; Liu, D.; Razal, J.M.; Lei, W. Interfacial engineering of 3D hollow Mo-based carbide/nitride nanostructures. *ACS Appl. Mater. Interfaces* **2021**, *13*, 50524. [CrossRef]

22. Available online: https://www.iris-france.org/wp-content/uploads/2019/01/Policy-PAPER-GENERATE-janvier-2019.pdf (accessed on 31 January 2019).

23. Cauchetier, M.; Croix, O.; Luce, M.; Michon, M.; Paris, J.; Tistchenko, S. Laser synthesis of ultrafine powders. *Ceram. Int.* **1987**, *13*, 13. [CrossRef]

24. Cauchetier, M.; Croix, O.; Herlin, N.; Luce, M. Nanometric Si/C/N powder production by laser-aerosol interaction. *J. Am. Ceram. Soc.* **1994**, *77*, 993. [CrossRef]

25. Belchi, R.; Habert, A.; Foy, E.; Gheno, A.; Vedraine, S.; Antony, R.; Ratier, B.; Bouclé, J.; Herlin-Boime, N. One-step synthesis of TiO$_2$/graphene nanocomposites by laser pyrolysis with well-controlled properties and application in perovskite solar cells. *ACS Omega* **2019**, *4*, 11906. [CrossRef]

26. Yuan, S.; Xu, S.; Liu, Z.; Huang, G.; Zhang, C.; Ai, J.; Li, X.; Li, N. Ultra-small molybdenum carbide nanoparticles in situ entrapped in mesoporous carbon spheres as efficient catalysts for hydrogen evolution. *ChemCatChem* **2019**, *11*, 2643. [CrossRef]

27. Liu, Y.; Yu, G.; Li, G.D.; Sun, Y.; Asefa, T.; Chen, W.; Zou, X. Coupling Mo$_2$C with nitrogen-rich nanocarbon leads to efficient hydrogen-evolution electrocatalytic sites. *Angew. Chem. Int. Ed.* **2015**, *54*, 10752. [CrossRef] [PubMed]

28. Chen, Y.Y.; Zhang, Y.; Jiang, W.J.; Zhang, X.; Dai, Z.; Wan, L.J.; Hu, J.S. Pomegranate-like N,P-doped Mo$_2$C@C nanospheres as highly active electrocatalysts for alkaline hydrogen evolution. *ACS Nano* **2016**, *10*, 8851. [CrossRef] [PubMed]

29. Wu, Z.Y.; Hu, B.C.; Wu, P.; Liang, H.W.; Yu, Z.L.; Lin, Y.; Zheng, Y.R.; Li, Z.; Yu, S.H. Mo$_2$C nanoparticles embedded within bacterial cellulose-derived 3D N-doped carbon nanofiber networks for efficient hydrogen evolution. *NPG Asia Mater.* **2016**, *8*, e288. [CrossRef]

30. Chen, L.; Jiang, H.; Jiang, H.; Zhang, H.; Guo, S.; Hu, Y.; Li, C. Mo-based ultrasmall nanoparticles on hierarchical carbon nanosheets for superior lithium ion storage and hydrogen generation catalysis. *Adv. Energy Mater.* **2017**, *7*, 1602782. [CrossRef]

31. Yan, H.; Xie, Y.; Jiao, Y.; Wu, A.; Tian, C.; Zhang, X.; Wang, L.; Fu, H. Holey reduced graphene oxide coupled with an Mo$_2$N–Mo$_2$C heterojunction for efficient hydrogen evolution. *Adv. Mater.* **2018**, *30*, 1704156. [CrossRef]

32. Wei, H.F.; Xi, Q.Y.; Chen, X.A.; Guo, D.Y.; Ding, F.; Yang, Z.; Wang, S.; Li, J.; Huang, S.M. Molybdenum carbide nanoparticles coated into the graphene wrapping N-doped porous carbon microspheres for highly efficient electrocatalytic hydrogen evolution both in acidic and alkaline media. *Adv. Sci.* **2018**, *5*, 1700733. [CrossRef]

33. Wu, C.; Liu, D.; Li, H.; Li, J. Molybdenum carbide-decorated metallic cobalt@nitrogen-doped carbon polyhedrons for enhanced electrocatalytic hydrogen evolution. *Small* **2018**, *14*, 1704227. [CrossRef] [PubMed]

34. Wang, Y.; Zhu, S.; Tsubaki, N.; Wu, M. Highly dispersed Mo$_2$C anchored on N,P-codoped graphene as efficient electrocatalyst for hydrogen evolution reaction. *ChemCatChem* **2018**, *10*, 2300. [CrossRef]

35. Ouyang, T.; Ye, Y.Q.; Wu, C.Y.; Xiao, K.; Liu, Z.Q. Heterostructures composed of N-doped carbon nanotubes encapsulating cobalt and β-Mo$_2$C nanoparticles as bifunctional electrodes for water splitting. *Angew.Chem. Int. Ed.* **2019**, *58*, 4923. [CrossRef] [PubMed]

36. Geng, D.; Zhao, X.; Chen, Z.; Sun, W.; Fu, W.; Chen, J.; Liu, W.; Zhou, W.; Loh, K.P. Direct synthesis of large-area 2D Mo$_2$C on in situ grown graphene. *Adv. Mater.* **2017**, *29*, 1700072. [CrossRef] [PubMed]

37. Bi, X.X.; Das Chowdhury, K.; Ochoa, R.; Lee, W.T.; Bandow, S.; Dresselhaus, M.S.; Eklund, P.C. Structural characterization of nanocrystalline Mo and W carbide and nitride catalysts produced by CO$_2$ laser pyrolysis. *MRS Online Proc. Libr.* **1994**, *368*, 69. [CrossRef]

38. Ochoa, R.; Hager, G.T.; Lee, W.T.; Bandow, S.; Givens, E.; Eklund, P.C. Relative activity and selectivity of nanoscale Mo$_2$N, Mo$_2$C and MoS$_2$ catalysts synthesized by laser pyrolysis. *MRS Online Proc. Libr.* **1994**, *368*, 27. [CrossRef]

39. Ochoa, R.; Bi, X.X.; Rao, A.M.; Eklund, P.C. *The Chemistry of Transition Metal Carbides and Nitrides*; Oyama, S.T., Ed.; Springer: Dordrecht, The Netherlands, 1996; p. 489.

40.   Roisnel, T.; Rodriguez-Carvajal, J. WinPLOTR: A Windows tool for powder diffraction patterns analysis Materials Science Forum. In *Materials Science Forum*; Transtec Publications: Freienbach, Switzerland, 1999; pp. 118–123.

41.   Rodríguez-Carvajal, J. Recent Developments of the Program FULLPROF. In *Commission on Powder Diffraction (IUCr)*; Newsletter: London, UK, 2001; Volume 26, p. 12.

42.   Lin, L.; Zhou, W.; Gao, R.; Yao, S.; Zhang, X.; Xu, W.; Zheng, S.; Jiang, Z.; Yu, Q.; Li, Y.W.; et al. Low-temperature hydrogen production from water and methanol using Pt/α-MoC catalysts. *Nature* **2017**, *544*, 80. [CrossRef]

43.   Baek, D.S.; Jung, G.Y.; Seo, B.; Kim, J.C.; Lee, H.W.; Shin, T.J.; Jeong, H.Y.; Kwak, S.K.; Joo, S.H. Ordered mesoporous metastable α-MoC$_{1-x}$ with enhanced water dissociation capability for boosting alkaline hydrogen evolution activity. *Adv. Funct. Mater.* **2019**, *29*, 1901217. [CrossRef]

44.   Hu, M.; Chen, H.; Liu, B.; Xu, X.; Cao, B.; Jing, P.; Zhang, J.; Gao, R.; Zhang, J. Coupling ceria with dual-phased molybdenum carbides for efficient and stable hydrogen evolution electrocatalysis at large-current-density in freshwater and seawater. *Appl. Catal. B* **2022**, *317*, 121774. [CrossRef]